Microstreaming Effects on Particle Concentration in an Ultrasonic Standing Wave

J. F. Spengler and W. T. Coakley
Cardiff University, School of Biosciences, PO Box 915, Cardiff CF10 3TL, U.K.

K. T. Christensen
University of Illinois, Laboratory for Turbulence and Complex Flow, Dept. Theoretical and Applied Mechanics, 216 Talbot Laboratory, 104 South Wright Street, Urbana, IL 61801

It is shown that the magnitude of Rayleigh microstreaming convective drag on microparticles in water in a 3.2-MHz ultrasonic standing wave can be comparable to the lateral direct radiation force in the nodal plane (DRF_1) and can significantly influence the microparticle aggregation. The transducer of a single half-wavelength chamber was excited to give a single particle aggregate. The estimated sound pressure amplitude was 0.5 MPa. Particle image velocimetry (PIV) measurements gave the average microstreaming velocity in the nodal plane as 450 $\mu m \cdot s^{-1}$, which is comparable to the 340- $\mu m \cdot s^{-1}$ value calculated from Rayleigh's theory. Movement of 25-μm latex particles was primarily determined by DRF_1, while that of smaller 1.0 μm, particles was determined by Rayleigh microstreaming. A 15-μm latex particle velocity map, simulated from microstreaming data, the measured velocity map of 25-μm particles, and the cube-dependent relationship between DRF_1's on particles of different sizes, was in reasonable agreement with a measured velocity map. Further evidence for the importance of microstreaming came from the result that velocities for 1- and 25-μm particles were of similar magnitude, but were opposite in direction.

Introduction

It has been known for some time that particles in suspension exposed to an ultrasonic standing wave (USW) are driven by an axial direct radiation force (DRF_a) to concentrate at nodal or antinodal planes (Sollner and Bondy, 1936). The phenomenon has received significant attention in recent years in areas such as particle or cell harvesting from suspension (Cousins et al., 2000; Gupta and Feke, 1998; Groschl, 1998; Spengler et al., 2001), particle separation (Yasuda et al., 1996), and noncontact manipulation of microparticles in immunoagglutination assays (Gray et al., 1999).

This axial radiation force DRF_a that drives spheres of volume V, density ρ_p, and compressibility β_p to a node or antinode plane in a liquid of density ρ_o and compressibility β_o can be derived from the particle potential energy expression of Gor'kov (1962), as

$$DRF_a = -\pi P_o^2 V \beta_o/(2\lambda)\cdot\phi(\beta,\rho)\cdot\sin(4\pi z/\lambda) \qquad (1)$$

where P_o is the sound pressure amplitude, z is the distance from a pressure node, and λ is the wavelength of the driving frequency in water. The contrast factor ϕ is

$$\phi = (5\rho_p - 2\rho_o)/(2\rho_p + \rho_o) - \beta_p/\beta_o \qquad (2)$$

Particles with positive-contrast factor are driven toward a pressure node, while particles for which ϕ is negative are driven toward the antinode. Particles subsequently move within the plane to give "columns" of particle aggregates at half wavelength intervals in the axial direction. The process is shown in Figure 1.

Lateral variations in the field distribution within the nodal planes give rise to a lateral radiation force DRF_1, of the same

Correspondence concerning this article should be addressed to W. T. Coakley. Current address of J. F. Spengler: Gelsenwasser AG, Abt PIA, Willy-Brandt-Allee 26, D-45891 Gelsenkirchen, Germany.
Current address of K. T. Christensen: University of New Mexico, Dept. Mechanical Engineering, ALbuquerque, NM 87131.

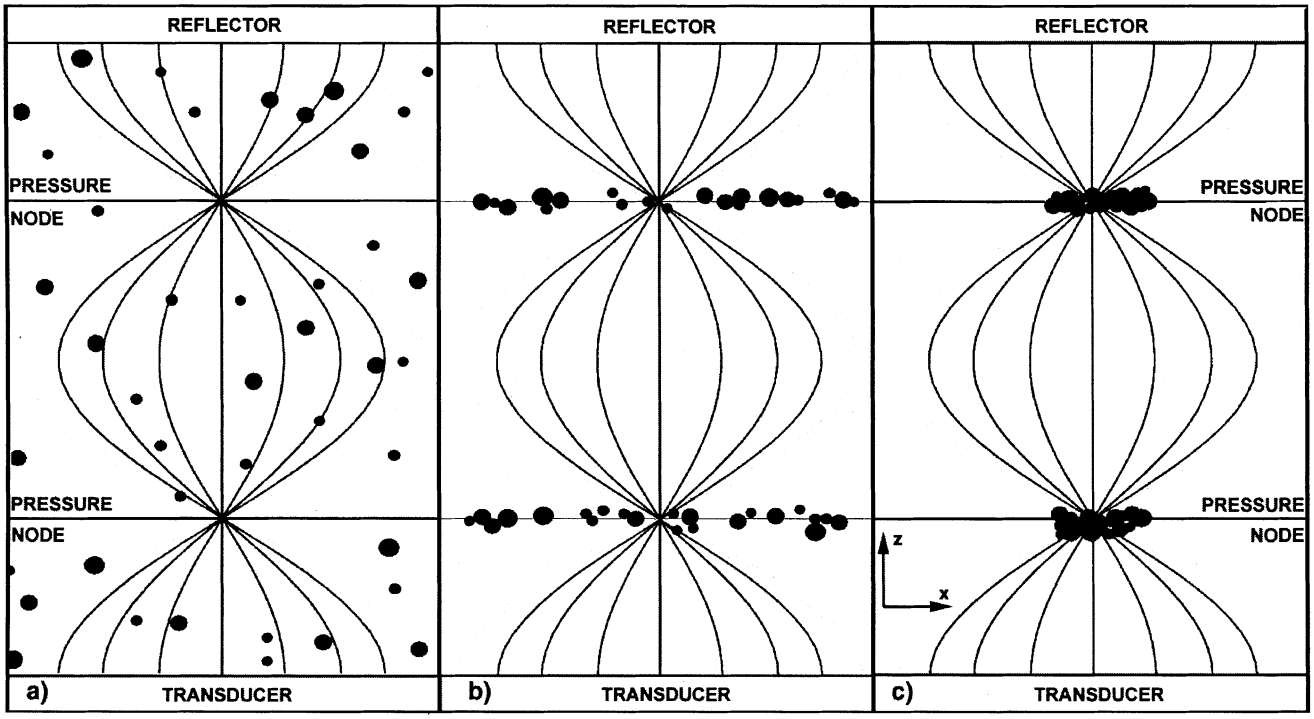

Figure 1. Temporal progression of suspended particle aggregation in a USW.

(a) Particles are initially homogeneously distributed in suspension; (b) particles move within seconds to concentrate in the nodal planes; (c) in the following tens of seconds the particles concentrate in clumps within the nodal planes. The distance between transducer and reflector is one wavelength, so there are two pressure nodes in the chamber.

origin as DRF_a, causing particles to clump within the plane. (Pressures are not everywhere zero in the nodal plane because of near-field and boundary effects.) Numerical calculation of the DRF potential according to Gor'kov's (1962) theory has been carried out by Johring (1998). He assumed a piston excitation in an unbounded water volume. It can be estimated from his results that the force is considerably stronger in the axial direction than in the lateral. This is in agreement with measurements of axial and lateral DRF force distributions (Tuziuti et al., 1999; Woodside et al., 1997; Yasuda, 1999), showing that the force in the lateral direction is about 100 times weaker than the axial component of the DRF.

In addition to forces on suspended particles, acoustic streaming is induced in the suspending phase. This streaming exerts a drag on a particle and would be expected to modify particle behavior. Streaming arises because of energy dissipation mechanisms in the bulk phase due to energy absorption in the fluid and because of dissipation at the interfaces between the fluid and solid surfaces. Zarembo (1971) distinguished between large-scale Eckart streaming (scale $\gg \lambda$) and two types of small-scale microstreaming: (1) Rayleigh streaming (scale approx. $= \lambda$) and (2) boundary layer Schlichting streaming (scale $\ll \lambda$). Eckart streaming and thermal convection can drive particles out of desired positions or disrupt particle aggregates. Spengler and Jekel (2000) have shown that a short container dimension along the sound axis effectively eliminates large-scale streaming.

Microstreaming occurs generally due to energy dissipation in the viscous boundary layer of the waveguide and other solid surfaces present. Rayleigh (1945) treated the case where a

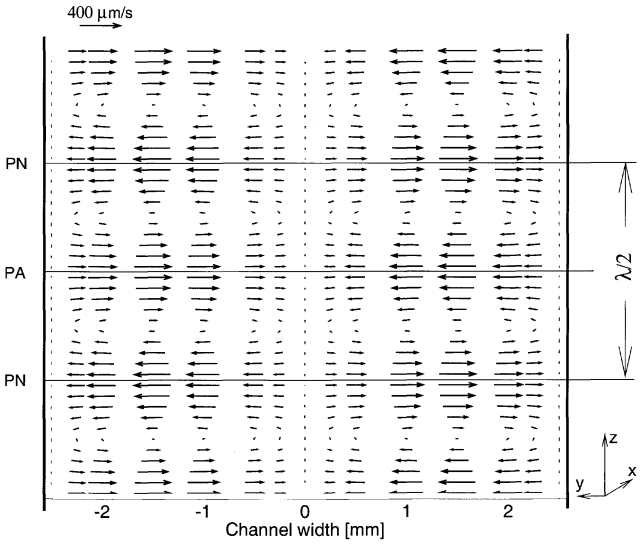

Figure 2. Rayleigh microstreaming between parallel walls (Eqs. 3a and 3b); 5-mm channel width, 1.93 MHz, 1 MPa in water, *z*-axis stretched by a factor of 50, PN pressure node, PA antinode.

plane standing wave is situated between parallel walls (Figure 2). The sound propagation direction is parallel to the walls (z-direction). The spacing between the walls is assumed to be wider than the wavelength ($2y_1 \gg \lambda$) and the wavelength

longer than the acoustic boundary-layer thickness ($\lambda \gg \delta$), where y_1 is the channel half-width when the origin of the y coordinate is in the center. The velocity components (in the lateral, that is, y-direction) and u_z (in the z-direction), have the following form (v_0 acoustic particle displacement velocity, c_0 speed of sound)

$$u_y(y,z) = -\left(6\pi v_0^2 f/16c_0^2\right)\cdot\left(y - y^3/y_1^2\right)\cdot\cos(4\pi zf/c_0) \tag{3a}$$

$$u_z(y,z) = -\left(3v_0^2/16c_0\right)\cdot\left(1\text{-}3y^2/y_1^2\right)\cdot\sin(4\pi zf/c_0) \tag{3b}$$

Figure 2 shows the streaming pattern calculated according to Eqs. 3. The lateral dimension between the two parallel walls is 5 mm. Four pairs of vortices are seen in the one wavelength chamber. There are two pressure nodal planes (PN) where particles gather under the action of the axial DRF. Integration and averaging of Eq. 3a over the channel halfwidth gives the average lateral velocity in the pressure node plane as

$$u_{y,av} = \left(3\pi v_0^2 f\right)/\left(32c_0^2\right)y_1 \tag{4}$$

Schlichting microstreaming is essentially a vortex flow inside the viscous boundary. It has the same origin as outside-boundary Rayleigh streaming discussed earlier (Zarembo, 1971) and rotates in the counterdirection. The boundary-layer thickness, δ, is defined as $\delta = (v/\pi f)^{0.5}$, where v is kinematic viscosity and f is the frequency. The boundary-layer thickness, for a 3-MHz field in water, the situation in this work, is about 0.22 μm, while the thickness of the vortex is about 1.9δ. This thickness is well below the resolution of the optical and microscopic methods employed here, so Schlichting streaming will not be considered further.

Gould and Coakley (1974) and Coakley et al. (1989) examined the contribution of Rayleigh microstreaming in the axial direction to the net force on a particle moving to the pressure node. Spengler et al. (2001) recently drew attention to the influence of lateral Rayleigh microstreaming on the movement of particles within the nodal planes. Their investigation was stimulated by the work of Woodside et al. (1997), who had earlier suppressed Eckart streaming in a carefully designed chamber and then identified the contribution of DRF_1 to particle movement and aggregation within the planes. Spengler et al. (2001) employed a macrolens system and a dedicated microscope setup to investigate clump formation in a "minichamber" that had an acoustic path length of one wavelength at 1.93 MHz, and in which the sound pressures were typical of operational ultrasonic cell separation devices (Oudshoorn et al., 1999; Hawkes and Coakley, 1996). The velocities of yeast cells (*Saccharomyces cerevisiae*) in the standing-wave field were measured by microscope particle image velocimetry (PIV) techniques. It was observed that cells were quickly driven into the pressure node planes by the axial DRF. However, within these planes many cells did not directly approach the putative aggregation regions, but were dragged around by streaming before being driven "off camera" where small aggregates formed that then moved toward the principal aggregation regions where large clumps were building up. The scale of the streaming patterns observed (of the order of one wavelength) matched that of Rayleigh microstreaming. And the measured cell velocity (0.4 mm$\cdot$s^{-1}) was in reasonable agreement with values calculated from Rayleigh's theory. Thus, microstreaming was shown to be important in small ultrasonic chambers, where large-scale Eckart streaming was ruled out. The work had shown that both DRF and microstreaming contributed to yeast aggregate formation. The authors hypothesized that the systems employed might quantitatively separate the contributions of the two mechanisms by employing small latex particles as microstreaming tracers while highlighting DRF effects with larger particles that would be much more strongly influenced by the volume-dependent DRF_1 force.

This hypothesis was tested in the experiments described here. A single half-wavelength chamber with one principal central particle concentration region was developed. The approach thereafter was to observe the behavior of differently sized particles under identical sonication conditions and to measure their velocities with the PIV method. One-micrometer particles were employed as tracers for the microstreaming present. The DRF distribution was deduced from the behavior of 25-μm particles, where the contribution of the microstreaming drag can be estimated from the streaming-field information given by the small particles experiments. "Medium-sized" (15-μm) particles showed similar order-of-magnitude influences of both DRF and microstreaming. The velocities to be expected of these particles were then simulated with a force-balance approach, which considered the microstreaming drag (from 1-μm experiments), the Stokes drag force and the DRF (from 25-μm experiments). These calculations showed reasonable agreement with the experimental data, thus confirming that DRF and microstreaming drag are main influences on particle behavior in short path length systems. The experimental setup and analysis methods described in the following provide a new powerful system for general studies of USW particle manipulation mechanisms.

Materials and Methods

Minichamber/microscope set-up

The acoustic minichamber employed in the present work had three essential components: a transducer, a spacer that determined the acoustic path length, and a reflector. These were secured between the bottom and top parts of the minichamber by four screws.

The transducer had a nominal resonance of 3 MHz. Its electrodes were etched to give a 10×10 mm^2 area on the aqueous-load side of the transducer and a 6-mm-dia. circle on its back. A similar back-electrode layout was previously employed to produce an axial column of aggregated particle clumps in a multiwavelength chamber (Whitworth and Coakley, 1992). The intention here was to produce a single clump of particles for microscopic examination in a single half-wavelength chamber. The 0.25-mm-thick stainless steel spacer formed a 10-mm-wide channel between the transducer and reflector and also determined the acoustic path length in the aqueous phase. A quartz glass acoustic reflector provided optical access to the chamber from above. Its 1.48-mm thickness was chosen for optimum reflection properties (integer multiples of $\lambda/4$). The frequency at which the acoustic path length

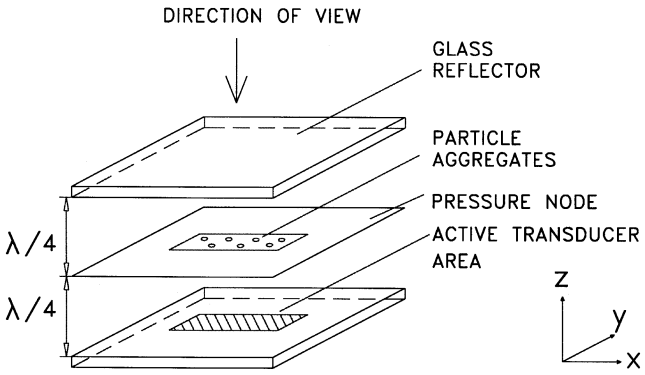

Figure 3. The essential components of the half-wavelength minichamber, showing the transducer, reflector, and the single nodal plane toward which suspended particles move initially.

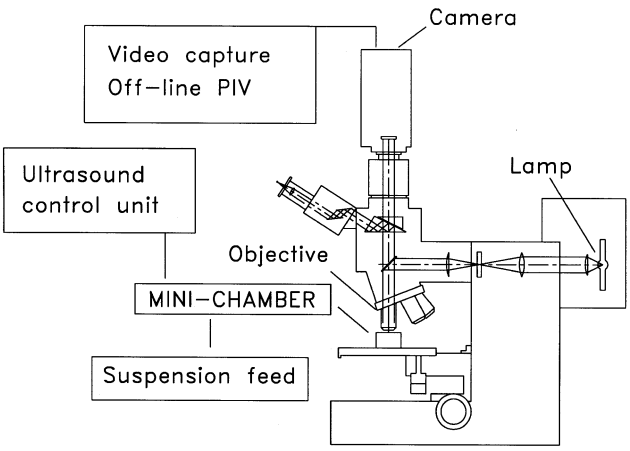

Figure 4. The experimental assembly (adapted from Spengler et al., 2001).

The 3-MHz single half wavelength minichamber is on the microscope stage. A peristaltic pump fed the suspension to the minichamber. The ultrasound control unit tracked a preselected voltage maximum and maintained the drive frequency at that point. PIV analysis was performed off-line with the software package PIV Sleuth (Christensen et al., 2000).

was exactly one half-wavelength, that is, one pressure nodal plane, in the chamber is designated the "chamber resonance." The chamber resonance was close to the transducer thickness resonance. The transducer reflector and single pressure node for particle concentration are shown in Figure 3.

Observation in the direction of the sound propagation (z-) axis was performed with an Olympus BX 40 epifluorescence-microscope with a 10 times objective. A PAL CCD camera (Fujitsu) was connected via an $\times 0.5$ microscope-TV adaptor that gave a field of view of about 1.3×1.0 mm^2. Video sequence recording onto tape and PC has previously been described (Spengler et al., 2001). Figure 4 shows the experimental setup.

Suspensions

The model particles employed were dried yeast resuspended in tap water (*S. cerevisiae*; Allinson, Maidenhead, U.K.), or either white or fluorescent latex spheres (Table 1). The latter were employed to give high particle-image contrast against an essentially black background. Particles were suspended in tap water. The unit volume concentrations of the larger particles were estimated from hemocytometer counts. The concentrations (% volume) of smaller particles was lower than those for larger particles in order to maintain a broadly similar number of particles per unit volume while retaining a suspension of single particles for the early stages of the particle velocity determinations.

Ultrasound generation

A sine wave, generated by a function synthesizer [Hewlett-Packard (HP)], went to an RF amplifier (ENI 2100L, ENI, Rochester, NY). The amplifier output voltage applied to the transducer on load was monitored on an oscilloscope. USW control was maintained by computerized tracking of the driving frequency. The software STAND scans voltage-frequency spectra from a voltmeter and allows the frequency to be held on either a transducer voltage maximum or minimum (Hawkes and Coakley, 1996). Each experiment was repeated at least three times under the same conditions. No significant difference in results between these repetitions was detected.

Figure 5 shows a typical voltage scan of the transducer of the "single-trap" minichamber. The three pairs of pronounced minima and maxima were tracked individually by the STAND software. Figure 6 shows that distinctively different patterns of yeast clumps had arisen in 100-s sonication at the frequencies associated with each of the six extreme voltages. An essentially single clump in the center of the volume was formed when the chamber was driven at the second voltage maximum, which corresponds to a drive frequency of about 3.17 MHz. This second voltage maximum was the frequency tracked for the minichamber experiments below.

Sound pressure and acoustic velocity estimation

The sound pressure and the acoustic displacement velocity in the acoustic minichamber were estimated from levitation of a large (45-μm) latex sphere (Table 1). These large parti-

Table 1. White (nonfluorescent) and Fluorescent Latex Particles Employed

Source	Type	Color	Dia. (μm)	σ (%)
Polymer Labs., Church Stretton, UK	n/a	White	45	n/a
Polymer Labs., Church Stretton, UK	SP-1466	White	25.1	6
Molecular Probes, Eugene, Oregon	F-8837	Bright blue	15	3
Sigma, Poole, UK	L-9652	Red	1.06	2.5

Note: σ is the coefficient of variation.

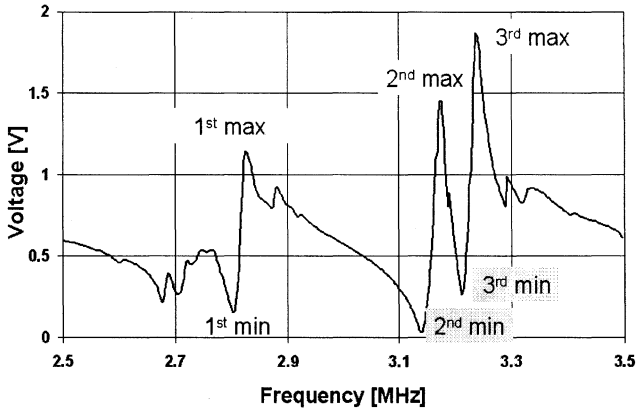

Figure 5. Frequency scan of transducer voltage for a fixed amplifier input signal.

cles were used, as they are influenced strongly by the DRF, which has a cubic dependence on particle diameter, d, while streaming drag is just linearly dependent on d. However, the particles were still small in comparison to the wavelength of the sound fields, as required for application of Gor'kov's (1962) DRF theory. A single sphere was held in suspension in the minichamber, with the sound on, and observed with the microscope. The voltage across the transducer was then lowered gradually until the buoyancy-corrected gravitational force $[F_g = (\rho_p - \rho_o) \cdot g \cdot V_p]$ was just balanced by the axial DRF (Eq. 1). This equivalence provided the value of P_o in Eq. 1. The values for the sound pressure and the acoustic particle velocity have been linearly extrapolated to the voltage levels employed operationally, since they both scale with the first power of the voltage.

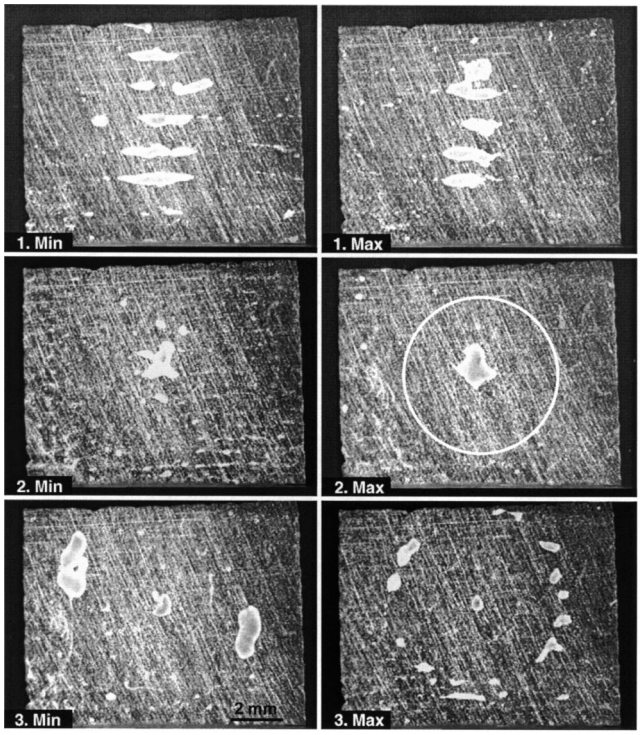

Figure 6. Yeast clump pattern formed at the voltage maxima and minima indicated after 100 s sonication: The circle on the "2nd max" detail shows the position of the circularly etched back electrode.

Experimental procedure

The microscope was prefocused on the central area in the pressure nodal plane. A peristaltic pump fed the suspension to the minichamber. Video recording and sonication began shortly after the pump was switched off (batch mode). The second voltage maximum (Figure 5) was tracked with a constant synthesizer voltage of 75 mV.

Micro-PIV analysis of particle movements

PIV analysis was performed off-line with the software package PIV Sleuth (Christensen et al., 2000) as described previously (Spengler et al., 2001). Vector validation was performed by removing vectors from regions with a signal-to-noise ratio below 100.

A small number ($n < 12$) of consecutive images were taken from the captured sequences and each half-frame was cross-correlated with its partner, resulting in $(n-1)$ PIV velocity maps. The velocity of the particles was assumed to be in steady state during this short time period (0.5 s maximum, 25-Hz full-frame rate). The particle velocity field was calculated by averaging the data for each individual vector point over the validated maps (Spengler, 2002). Thus, the random occurrence of low particle concentrations, which might result in invalid vectors in analyzed areas, was partly compensated. An upper limit of the standard error of the mean of 10% was defined as the maximum tolerable uncertainty of the measured velocity. Apparent outliers were removed manually. The standard error of the mean was minimized by repeating the experiment and averaging over the data gained from these repetitions. Out-of-focus particle images did not influence results here, as all particles were pushed, almost instantaneously, into the pressure node plane and were held in that plane.

Results

The experiments were performed at the second voltage maximum (Figure 5) of approximately 5 V (estimated sound pressure amplitude = 0.5 MPa). The occurrence of particle interaction was minimized by (1) the appropriate choice of particle concentration, and (2) the analysis of only the first 0.5 s of each experiment, where most particles were still separated and had not yet formed a significant number of clumps. Nyborg (1978) showed that interaction essentially can be neglected above particle separations larger than a particle diameter.

Rayleigh streaming traced by 1-μm fluorescent latex

The first six frames after sound was switched on were not analyzed, because the particles were not all yet in the prefocused nodal plane. The experiment was repeated 9 times and

the PIV Sleuth results of 45 vector maps averaged. The result is shown in Figure 7. The streaming flows laterally from a central "source" point, where the fluid streamed in the direction perpendicular to the paper plane, outwards toward the periphery of the sonicated volume. The maximum measured velocity at the upper edge of the field of view was about 150 $\mu m \cdot s^{-1}$. Few, if any, particles were left in the microscope field of view after 15 s. PIV analysis of a typical experiment showed no acceleration of the streaming during that 15-s period, suggesting that no significant thermal convective streaming built up in that time.

The 1-μm particles were not redelivered into the field of view. It was observed with the naked eye that these microparticles were transported to the edge of the active transducer area and remained there forming a "ring" of particles at the periphery of the chamber. This behavior can be explained with the different order of magnitude of the axial and the lateral DRF. While the lateral DRF is weak in comparison to the lateral streaming drag, so that the particles are dragged away by the flow, the axial DRF has been shown to be several orders of magnitude stronger than the lateral (Woodside et al., 1997; Tuziuti et al., 1999). When the particles approach the outer regions of the sonicated volume, where the lateral streaming velocity vanishes and the flow bends in the axial direction, it is plausible that the strong axial DRF holds the particles in the pressure node plane against the axial flow. Thus, 1-μm particles follow the streaming in the lateral direction, but not in the axial.

Aggregation of 25-μm latex

The first frame after sound was switched on was not included in the PIV analysis, because the particles were not all yet in the prefocused nodal plane. The experiment was repeated 22 times and the PIV Sleuth results of 220 vector maps averaged. This number of vector maps, which was considerably higher than in the 1-μm latex experiment cited earlier, were processed in order to bring the standard error of the mean under 10% in the lower "particle number" concentration of this experiment. The result is presented in Figure 8. It can clearly be seen that all particles headed toward the center of the field of view, where a clump was rapidly formed. Some particles approached the center along bent trajectories. This created two preferred directions of the particles' approach toward the center: from the upper and the lower edge of the field of view. The micrographs of Figure 9 show the particle distribution after two frames, when all of the particles are in the prefocused pressure node plane, and later details as the main aggregate grows by the addition of single beads or small clusters formed during movement in the pressure node plane. The 25-μm particles appear as bright dots encircled by dark rings under the lighting conditions present in the microscope employed. We note here that increasing the particle concentration leads to earlier formation of aggregates in suspension. These aggregates will experience an enhanced radiation force and, thus, come increasingly under the influence as DRF_I rather than streaming. In addition, Bjerknes forces will make a contribution to aggregation, but the importance of that contribution has not been assessed here.

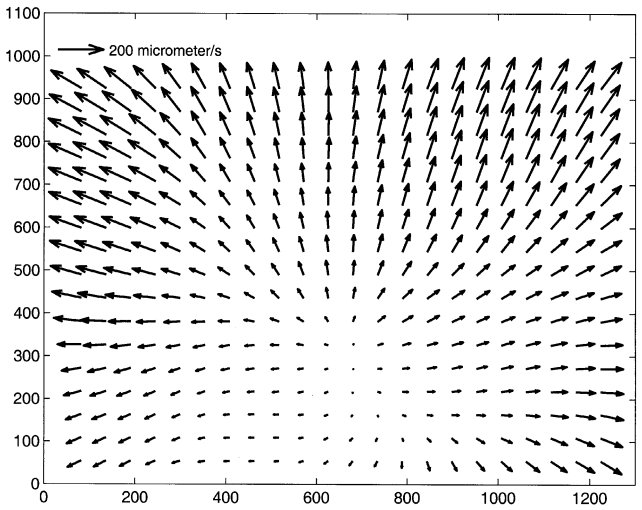

Figure 7. PIV analysis of 1-μm red fluorescent latex behavior.

The streaming "source" point is slightly off-axis of the field of view (pressure, 0.50 MPa, particle concentration 0.005% w/v).

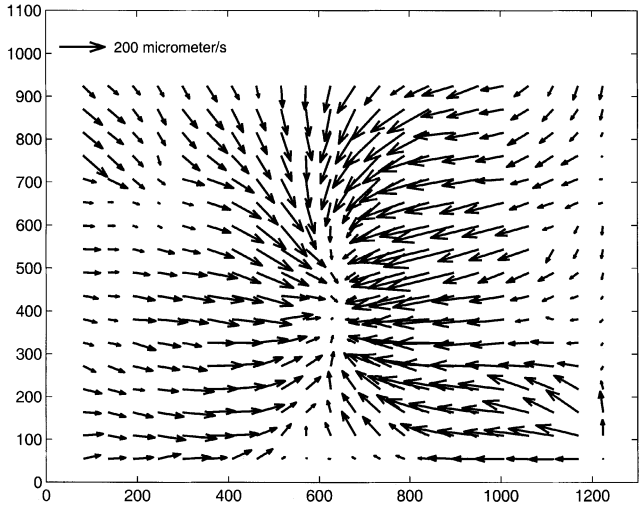

Figure 8. PIV analysis of 25-μm white latex behavior: pressure, 0.50 MPa; particle concentration, 0.15% w/v.

Aggregation of 15-μm latex

Figure 10 shows that the particle number in the field decreased during the first 12 s of exposure to ultrasound. Small clusters of spheres that had formed in the outer, off-camera parts of the chamber then began to enter the field of view and began to form an aggregate at the center of the field. This effect well illustrates the dependence of the DRF/Stokes-drag ratio on the particle or clump dimension. Once single particles, which were dragged away by the streaming, have come together in small aggregates, that have a larger "effective" size than the individual particles, the DRF eventually outweighs the streaming drag and these "primary"

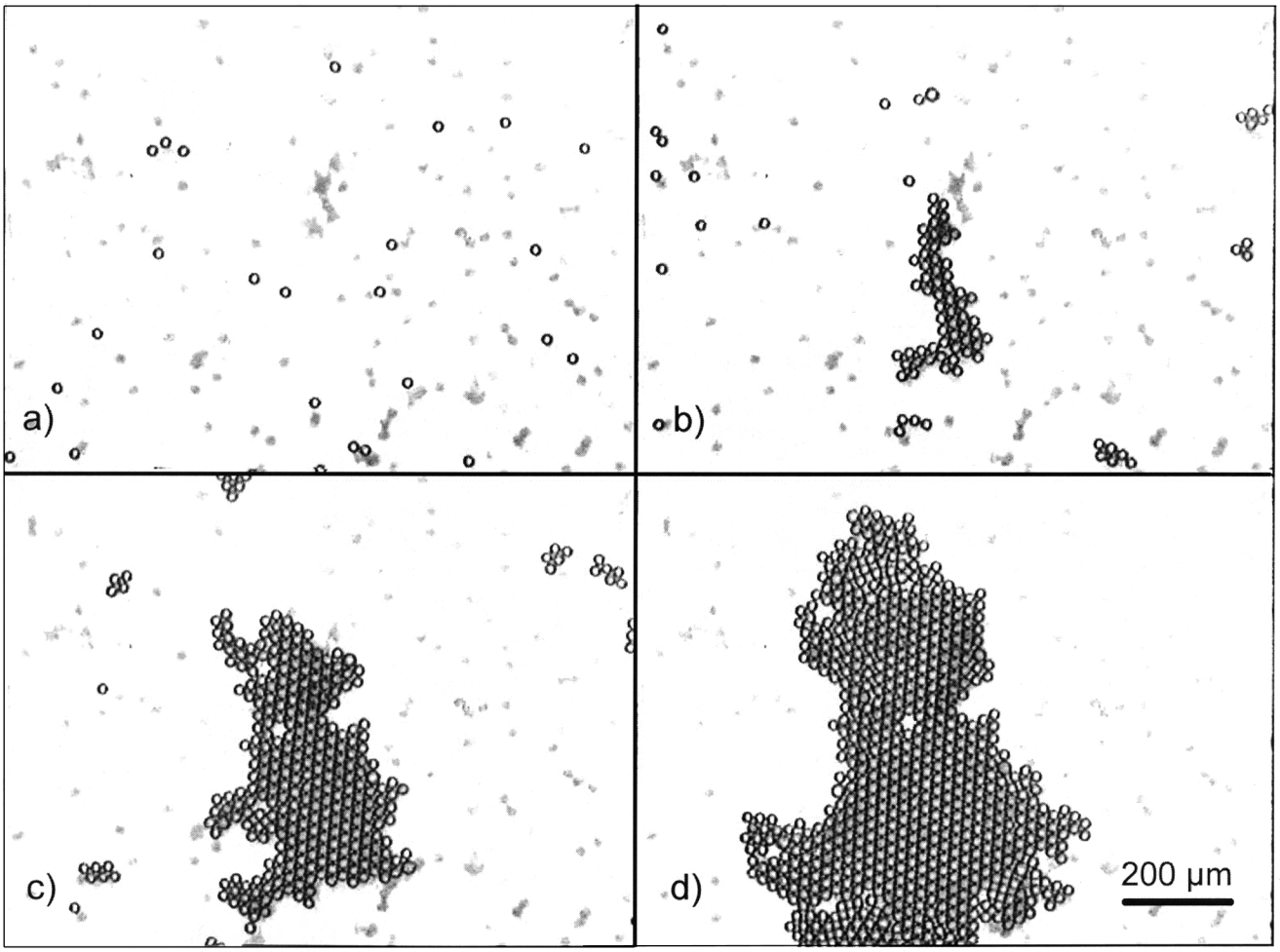

Figure 9. Development of an aggregate of 25-μm white latex particles at different times from switch-on.

(a) 0.08 s, the single particles are already in focus in the nodal plane; (b) 6 s, small aggregates formed off-screen enter the field and begin to contribute to the growth of the aggregate already formed from the single particles of (a); (c) 15 s, growth is largely by the inflow of clusters; (d) 37 s, aggregate growth is essentially completed.

aggregates or clusters are drawn into the center DRF potential well.

The PIV analysis for 15-μm beads is shown in Figure 11a. The first two frames after sound was switched on were not analyzed, because the particles were not all yet in the prefocused nodal plane. The experiment was repeated 30 times, and the PIV Sleuth results of 270 vector maps were averaged. This number of vector maps was necessary to reduce the standard error of the mean of the lower velocities of the 15-μm particles compared to those of the 1- and 25-μm particles (note that the reference vector in Figures 11a and 11b is 100 $\mu\text{m}\cdot\text{s}^{-1}$ rather than the 200 $\mu\text{m}\cdot\text{s}^{-1}$ of Figures 7 and 8. The error in the velocity map of Figure 11a could not be brought under 10% for all vectors, despite the high number of processed data. However, there is sufficient information to compare and discuss the theoretical and experimental results.

Discussion

The chamber

No comprehensive theory for the prediction of the pressure distribution in ultrasonicated fluid volumes is available yet, due to the extreme complex interactions between the geometrical container design, the boundaries, and the acoustic drive parameters. However, the modes excited in the system are closely connected to the mode distribution on the transducer surface, which can be changed by tuning the drive frequency, as investigated comprehensively both theoretically and with schlieren image techniques by Chinnery et al. (1997). These authors also found a dependence of the pressure distribution pattern on the actual sound pressure level in the volume, which becomes more "distorted" the higher the pressure level is. A thorough theoretical treatment of the DRF potential in the ideal plane, cylindrical, and spherical standing-wave fields for any modal combinations up to second-order excitation modes was conducted by Barmaz and Collas (1985). The authors showed that the excitation in the first axial rectangular (square transducer) and cylindrical mode (circular transducer) leads to an isolated potential well in the center of the nodal planes. In general, more potential wells, where particles are drawn in by the DRF, are seen with higher order and the overlay of several modes. The minichamber system described earlier, with its circular back electrode acts, when driven at the second maximum of its voltage scan (Figures 5 and 6) in a manner expected of a cylindrical system

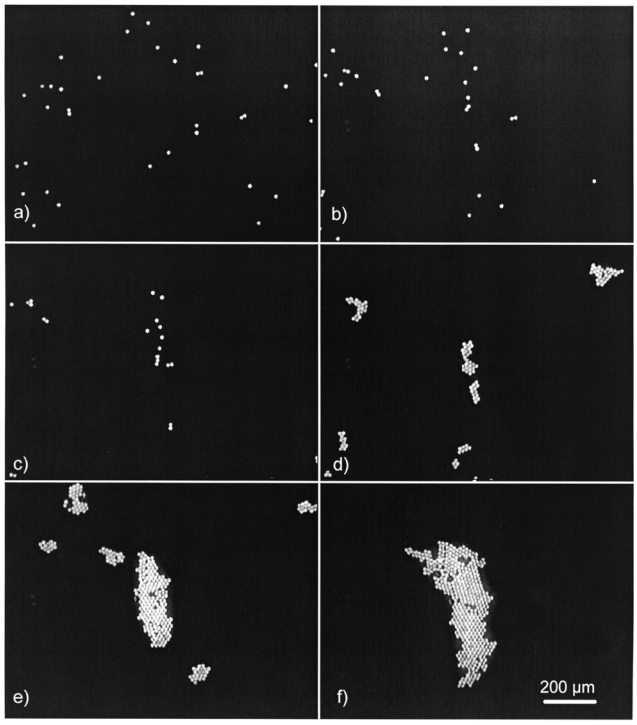

Figure 10. Development of an aggregate of 15-μm blue latex particles at different times from switch-on.

(a) 0.12 s, the spheres are in focus in the nodal plane; (b) 6 s and (c) 12 s, the number of particles in the field is decreasing; (d) 27 s and (e) 42 s, mini clusters, formed off screen, enter the field and form a growing aggregate; (f) the growth process is complete.

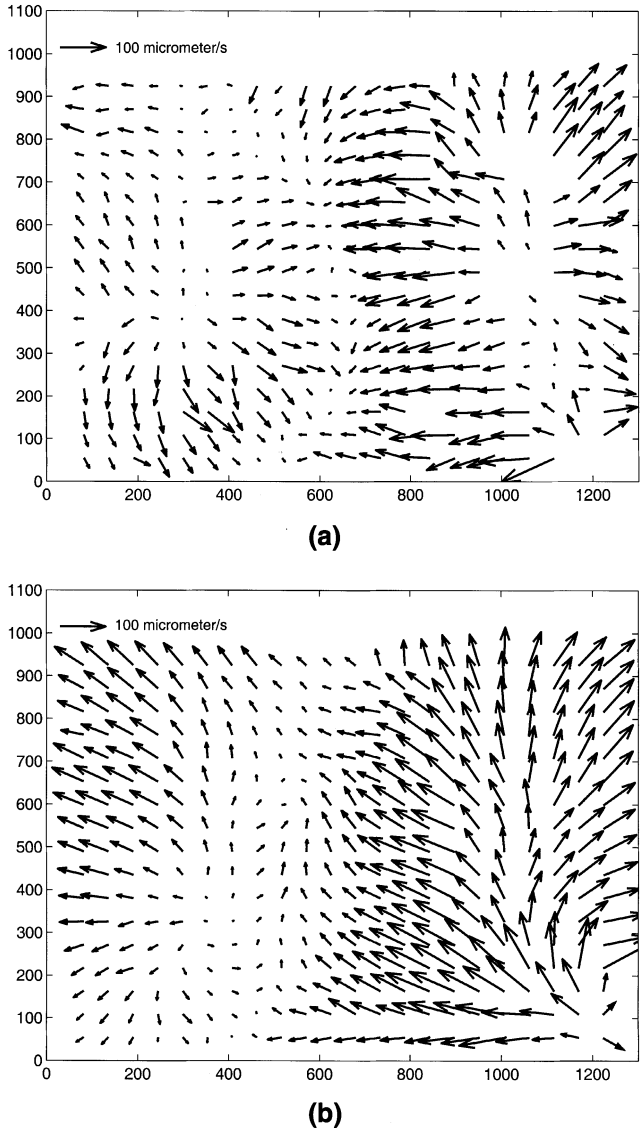

Figure 11. (a) PIV measurement of 15-μm latex movement in first 0.5 s of exposure to sound; (b) simulation of particle velocity vectors on the basis of the force balance discussed in text.

driven at its lowest (zero) mode (Whitworth and Coakley, 1992). Its "single well" characteristic has provided significant improvement on the experimental options offered by the multiwell chambers (Spengler et al., 2001).

Microstreaming

The average lateral Rayleigh microstreaming velocity, calculated from Eq. 4, gives a value of 340 $\mu m \cdot s^{-1}$ with the channel halfwidth of 5 mm, a value much higher than the 150-$\mu m \cdot s^{-1}$ maximum "field of view" value measured earlier. However, only 10% of the channel halfwidth is in the field of view. It can be estimated from a plot of Rayleigh velocity as a function of y (Spengler, 2002) that the average velocity is reached at about 30% of the chamber half-width, while the velocity increase up to that distance is essentially linear. This gives an extrapolated value of the average Rayleigh streaming velocity of 450 $\mu m \cdot s^{-1}$ (3×150 $\mu m \cdot s^{-1}$) that is of the same order of magnitude as the calculated value of 340 $\mu m \cdot s^{-1}$. It is noted here that the source point is shifted to the lower image edge and is not exactly central. The streaming field is perfectly symmetrical to the source point, which differs significantly from the expected pattern on the basis of the theoretical prediction of Rayleigh streaming between parallel walls (Figure 2). In that case, the flow would be symmetrical to the horizontal center-line of the chamber/ field of view. However, the flow field observed here matches precisely the radial streaming field in a pressure node of a standing wave in a cylinder, also treated by Rayleigh (1945). The derivation of the axial and radial velocity components is carried out in essentially the same way as that of Eqs. 3, but for cylindrical coordinates. The absolute values of the velocities do not, for similar geometric dimensions, differ much from that in the planar case. Thus, a detailed treatment of this cylindrical Rayleigh streaming is omitted here.

The order of magnitude of the microstreaming present under the operational sound-pressure conditions here is of the same order of magnitude as the velocity reported on large-scale streaming (Eckart and thermal) in high-volume, multi-wavelength industrial reactors. Johring (1998) estimated streaming velocities of the order of 1 $mm \cdot s^{-1}$ from video

records of the disruption of particle columns by large-scale streaming in a 0.5 L, 3-MHz batch system. Laser Doppler anemometry (LDA) measurements in a commercial USW cell filter by Mitome et al. (1997) showed the same order of magnitude (mm s^{-1}) under the operating conditions for the device. Thus, the considerable influence of microstreaming, which overlays the large-scale streaming in high volume systems, may be present in those systems.

The possibility that thermal streaming, generated by heat dissipation in the system, might have contributed to the motions involved was considered. An effective test, that is, inverting the resonator so that the transducer layer would be uppermost and transducer-induced thermal streaming would be suppressed, was not an option because of the structure of our microscope. It was noted, however, that, in the normal chamber configuration, microparticle movement stopped instantaneously (in less than one frame) when the sound was switched off. Streaming due to thermal gradients would not be expected to terminate so quickly. Hawkes et al. (1998) showed that thermal streaming was essentially eliminated in a 5-cm path length multiwavelength standing-wave system in the environment. More recent work with a chamber as described here showed that streaming patterns that have been observed at 1 g continued during the 20-s duration of exposure to microgravity (J. J. Hawkes, personal communication, 2001). This qualitative observation (a camera lens, rather than a microscope was employed to monitor the flow so that measurement of microparticle streaming speeds were not possible) is consistent with a situation where acoustic streaming rather than thermal streaming dominates in the short pathlength chamber used in the present study.

Simulation of the behavior of 15-μm latex and comparison with experimental data

The streaming field in the center of the minichamber is shown in Figure 7. The 25-μm latex particles investigated earlier (Figure 8) were mainly influenced by the DRF_1, but also experienced the streaming drag force. Woodside et al. (1997) presented a way to reconstruct the DRF potential field in a standing wave by analyzing the movement of 10-μm latex beads in the pressure node plane. The authors presented an equipotential plot of the area they observed. Not all particle trajectories analyzed were normal to the equipotential lines. This effect was attributed to the action of gravity. Microstreamimg had not been included in the analysis.

A prediction of the 15-μm particle behavior is made here from the suspending phase microstreaming data (Figure 7) and the behavior of 25-μm latex (Figure 8), without involving reconstruction of the DRF distribution. The only knowledge exploited is that the DRF is proportional to the volume of the particle. It is assumed that the relevant material properties of the three different size latex suspensions, which were supplied by three different manufacturers, are the same. The inertia of the particles can be neglected, since the time for a particle of the order of the size employed in this work to attain the final speed is below 0.1 ms (Woodside et al., 1997; Gould and Coakley, 1974). It is much shorter than the time resolution (40 ms) of the 25-Hz PAL video system employed. This simplifies the equation of motion for an individual particle from a second-order differential equation to a simple force balance, in which the sum of the lateral DRF vector (F_{RF}) and the microstreaming drag vector (F_{MS}) must be counterbalanced by the Stokes drag (F_{St}), that is

$$F_{RF} + F_{MS} = F_{St}$$

The Stokes and the microstreaming drag force are proportional to the particle diameter, d_p, as well as the velocity of the particle v_p, and the microstreaming velocity, v_{MS}, respectively

$$F_{St} = A \cdot d_p \cdot v_p$$

$$F_{MS} = A \cdot d_p \cdot v_{MS}$$

where A is the suspending phase-dependent proportionality factor. The microstreaming velocity can be set equal to the measured velocity of the 1-μm particles, and, thus, the expression for the DRF acting on 25-μm particles becomes

$$F_{RF,25} = A \cdot d_{25} \cdot (v_{25} - v_1) \tag{5}$$

The ratio of the DRFs on differently sized (diameters d_{25} and d_{15}), but otherwise identical particles depends, under the same acoustic conditions, on the cube of the ratio of the particle diameters, that is

$$F_{RF,15} = (d_{15}/d_{25})^3 \cdot F_{RF,25} = A \cdot d_{15} \cdot (v_{15} - v_1) \tag{6}$$

Equation 5 is now inserted into Eq. 6. Rearrangement gives

$$v_{15} = (15/25)^2 \cdot (v_{25} - v_1) + v_1 \tag{7}$$

The result of processing Eq. 7 with the data presented for 1- and 25-μm latex particles is illustrated in Figure 11b. The tendencies of the particle movements in both calculated and measured cases show reasonable agreement over much of the velocity map. Apparently random deviations between theory and experiment are seen in the upper center and the lower left part of the graphs. Some other scattered differences in the predicted and measured velocities occur. The predicted velocities generally are higher than the actual measured values. The differences are best seen in the upper left corner of Figures 11a and 11b. This difference suggests a systematic error in the calculation.

A number of error sources in the approach presented have to be considered. It has been assumed that the material properties of the three different particle sizes employed, which came from different companies, are identical, since the manufacturers were unable to provide material data on their individual products. Variation in size within the bead populations may also influence the experimental accuracy, especially in the case of 25-μm latex (Table 1). It also cannot be completely ruled out that particle–particle interactions and clumping occurred to some extent in the analyzed sequences, despite the fact that a very short time period (0.5 s maximum) at the beginning of the sonication was processed.

Figure 12 presents estimates of the average Rayleigh streaming drag force, the DRF_1 and the ratio of these forces

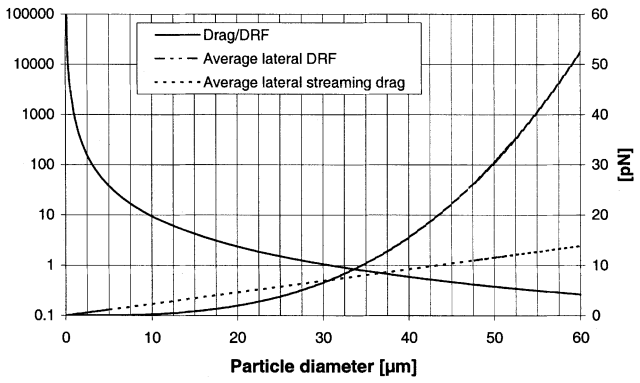

Figure 12. Estimates of the ratio of the average Rayleigh streaming drag and DRF_1 on latex spheres of different sizes for the experimental parameters assessed here.

as a function of latex particle size. The streaming velocity assumed was 50 $\mu m \cdot s^{-1}$, which is of the order of magnitude seen in the center of the field of view (Figure 7). DRF_1 was estimated, in line with results from other work referred to earlier (for example, Woodside et al., 1997), to be 0.01 times the DRF calculated from Eq. 1. The ratio of drag to DRF_1 (Figure 12) has a general form consistent with the results here, where radiation force and streaming control the velocities of the largest and smallest particles, respectively, while intermediate-sized particles (15 μm), where the competing vectors become comparable in magnitude, have the smallest velocity magnitude of the three. The figure gives the ratio drag:DRF_1 = 1.0 for particles of about 30 μm, which is larger than expected from our results, but falls generally within the tolerance of the assumptions made in constructing Figure 12. We note also that streaming drag and DRF_1 are both functions of z, and while the functional dependence is known for Rayleigh streaming, the same is not the case for the DRF_1. Since the acoustic radiation force is proportional to ultrasound frequency and energy dissipation in the system is proportional to frequency squared, a comparison of the frequency dependence of the relative effects of radiation pressure on the same-sized particles would be of interest. The results presented here emphasize the need to consider microstreaming as well as radiation force when investigating applications of the noncontact manipulation of suspended microparticles provided by megahertz frequency ultrasonic standing waves.

Acknowledgments

The authors are happy to acknowledge the support and interest of Prof. R. J. Adrian in this work. JFS was funded from EU TMR contract #ERBFMRXCT97-0156 UltraSonoSep.

Literature Cited

Barmaz, M., and P. Collas, "Acoustic Radiation Potential on a Sphere in Plane, Cylindrical and Spherical Standing Wave Planes," *J. Acoust. Soc. Amer.*, **77**, 928 (1985).

Chinnery, P. A., V. F. Humphrey, and C. Beckett, "The Schlieren Image of Two-Dimensional Ultrasonic Fields and Cavity Resonances," *J. Acoust. Soc. Amer.*, **101**, 250 (1997).

Christensen, K. T., S. M. Soloff, and A. J. Adrian, "PIV Sleuth: Integrated Particle Image Velocimetry Interrogation/Validation Software," TAM (Theoretical and Applied Mechanics) Report, University of Illinois at Urbana-Champaign, p. 943 (2000).

Coakley, W. T., D. W. Bardsley, F. Zamani, and D. J. Clarke, "Cell Manipulation in Ultrasonic Standing Wave Fields," *J. Chem. Tech., Biotechnol.*, **4**, 43 (1989).

Cousins, C. M., P. Holownia, J. J. Hawkes, M. S. Limaye, C. P. Price, P. J. Keay, and W. T. Coakley, "Plasma Preparation from Whole Blood Using Ultrasound," *Ultrasound Med. Biol.*, **26**, 881 (2000).

Gor'kov L. P., "On the Forces Acting on a Small Particle in an Acoustical Field in an Ideal Fluid," *Sov. Phys.—Doklady*, **6**, 773 (1962).

Gould, R. K., and W. T. Coakley, "The Effects of Acoustic Forces on Small Particles in Suspension," *Symp. on Finite Amplitude Wave Effects in Fluids*, Pergamon Press, Guildford, UK, p. 252 (1974).

Gray, S. J., M. A. Sobanski, E. B. Kaczmarski, M. Guiver, W. J. Marsh, R. Borrow, R. A. Barnes, and W. T. Coakley, "Ultrasound-Enhanced Latex Immunoagglutination and PCR as Complementary Methods for Non-Culture Based Confirmation of Meningococcal Disease," *J. Clin. Microbiol.*, **37**, 1797 (1999).

Groschl, M., "Ultrasonic Separation of Suspended Particles—Part {I}: Fundamentals," *Acustica*, **84**, 432 (1998).

Gupta, S., and D. L. Feke, "Filtration of Particulate Suspensions in Acoustically Driven Porous Media," *AIChE J.*, **44**, 1005 (1998)

Hawkes, J. J., and W. T. Coakley, "A Continuous Flow Ultrasonic Cell-Filtering Method," *Enzyme and Microb. Technol.*, **19**, 57 (1996).

Hawkes, J. J., J. J. Cefai, D. A. Barrow, W. T. Coakley and L. G. Briarty, "Ultrasonic Manipulation of Particles in Microgravity," *J. Phys. D*, **31**, 1673 (1998).

Johring, A., "Einsatz von Ultraschall zur Partikelagglomeration und fest-flussig Separation," Doctoral diss., Tech. Univ. of Berlin, Berlin, Germany (1998).

Mitome, H., T. Kozuka, T. Tuziuti, M. Groschl, B. Handl, and E. Benes, "Generation of Acoustic Streaming in an Ultrasonic Resonator for Particle Separation," *Proc. World Congress on Ultrasonics*, Yokohama, Japan, p. 200 (1997).

Nyborg, W. L., "Physical Principles of Ultrasound," *Ultrasound: Its Application in Medicine and Biology*, Vol. 1, F. J. Fry, Ed., Elsevier, Amsterdam, The Netherlands, p. 1 (1978).

Oudshoorn, A., F. Trampler, and B. Benes, "AppliSens Virtual Filter Perfusion—Ultrasonic Filtration System ADI 1015 BioSep," *BTI Biotech. Int.*, **11**, 27 (1999).

Rayleigh, J. W. S., *The Theory of Sound*, Vol. 2, Dover, New York (1945).

Sollner, K., and C. Bondy, "The Mechanism of Coagulation by Ultrasonic Waves," *Trans. Faraday Soc.*, **32**, 616 (1936).

Spengler, J., and M. Jekel, "Ultrasound Conditioning of Suspensions —Studies of Streaming Influence on Particle Aggregation on a Lab- and Pilot-Plant Scale," *Ultrasonics*, **38**, 624 (2000).

Spengler, J., F., M. Jekel, K. T. Christensen, R. J. Adrian, J. J. Hawkes, and W. T. Coakley, "Observation of Yeast Cell Movement and Aggregation in a Small-Scale MHz-Ultrasonic Standing Wave Field," *Bioseparation*, **9**, 329 (2001).

Spengler, J. F., "Applications of Ultrasonic Standing Waves for Suspended Particle Manipulation in the Water Industry," Doctoral Diss., Tech. of Univ. of Berlin, Berlin, Germany (2002).

Tuziuti, T., T. Kozuka, and H. Mitome, "Measurement of Distribution of Acoustic Radiation Force Perpendicular to Sound Beam Axis," *Jpn. J. Appl. Phys.*, **38**, 3297 (1999).

Whitworth, G., and W. T. Coakley, "Particle Column Formation in a Stationary Ultrasonic Field," *J. Acoust. Soc. of Amer.*, **91**, 79 (1992).

Woodside, S. M., B. D. Bowen, and J. M. Piret, "Measurement of Ultrasonic Forces for Particle-Liquid Separations," *AIChE J.*, **43**, 1727 (1997).

Yasuda, K., S. Umemura, and K. Takeda, "Particle Separation Using Acoustic Radiation Force and Electrostatic Force," *J. Acoust. Soc. Amer.*, **99**, 1965 (1996).

Yasuda, K., "Measurement of Microscopic Spatial Distribution of Acoustic Force Using Microspheres and Electrostatic Force," *Jpn. J. Appl. Phys.*, **38**, 3316 (1999).

Zarembo, L. K., "Acoustic Streaming," *High-Intensity Ultrasonic Fields*, Vol. 85, L. D. Rozenberg, ed., Plenum Press, New York, p. 137 (1971).

Manuscript received Oct. 10, 2002, and revision received Mar. 17, 2003.